MOLECULAR DYNAMICS STUDY ON THE EVAPORATION OF ETHANE, PROPANE AND THEIR MIXED FLUIDS AT THE COPPER SUBSTRATE

Jintao WU[1*#], Fu LIANG[2#], Xiaolin AO[1], Neng GAN[1], Wang XIE[1]

[*1] Chongqing Changzheng Heavy Industry Co., LTD., Chongqing 400083, China

[2] Key Laboratory of Low-grade Energy Utilization Technologies & Systems, Ministry of Education, Chongqing University, School of Energy and Power Engineering, Chongqing 400044, China

[*] Corresponding author; E-mail: 742978420@qq.com

[#] These authors contributed equally to this work

The organic Rankine cycle can harvest the cold energy from liquefied natural gas (LNG) by using non-azeotropic working fluids. The phase transition is one of the important processes in the thermodynamics cycles. In this paper, the interfacial evaporation characteristics of ethane, propane and their mixtures were investigated by molecular dynamics simulations. Several properties, including surface tension, diffusion coefficient, interaction energy were analyzed. The results show that the addition of ethane in the mixed working fluid increases the evaporation rate of propane, and the gas-liquid interfacial thermal resistance is relatively large in the total thermal resistance. The pure ethane system has the smallest thermal resistance, surface tension, intermolecular interaction energy and the largest diffusion coefficient, which make the evaporation energy barrier smaller.

Key words*: liquefied natural gas; mixed working fluid; evaporation; molecular dynamics*

1. Introduction

In recent years, with the continuous improvement of the level of science and technology, the economy has also developed rapidly. However, the energy crisis and environmental problems have become increasingly prominent. The emission of carbon dioxide, methane and other greenhouse gases is the main cause of global warming. Traditional fossil energy, such as coal and oil, has the disadvantages of high carbon emission and pollution. New energy sources (such as solar energy, wind energy, etc.) are still facing constraints such as instability and discontinuities.

Natural gas has the advantages of high calorific value and clean combustion products [1], which can be used as a high-quality resource at present and in the future. For long-distance transportation crossing the sea, the natural gas often will be cooled and compressed to form liquefied natural gas (LNG) [2]. When arriving at the receiving station, the LNG ships will transport the LNG from the cryogenic storage tank to the LNG regasification terminals, and then the LNG will be heated back to natural gas. LNG gasification at atmospheric pressure can release about 800 kJ/kg of cold energy [3]. However, currently, most LNG regasification terminals release cold energy directly into seawater or air, causing a large amount of cold energy waste. In response to this, researchers have proposed a large

number of LNG cold energy utilization methods, such as air separation, low temperature power generation, CO_2 capture, seawater desalination and so on [4-9].

Organic Rankine cycle (ORC) is a relatively mature LNG cold energy power generation technology [10]. In ORC, the working fluid is successively compressed, evaporated, expanded and condensed to generate power. The cycle has the advantages of simple process and relatively high efficiency, which has been widely used. Sun et al. [11] studied the optimization of three different ORC configurations (single-stage ORC, parallel two-stage ORC, and cascade two-stage ORC) using LNG cold energy. The results indicate that the parallel two-stage ORC is more suitable for lower heat source temperatures, while the cascade two-stage ORC performs better at higher heat source temperatures. Arcuri et al. [12] used LNG as the heat exchanger for Ocean Thermal Energy Conversion (OTEC) system and employed an Organic Rankine Cycle with ammonia as the working fluid for power generation through direct LNG expansion. Lee [13] optimized the cascaded Rankine cycle for cold energy recovery by applying a genetic algorithm. When used in ORC, LNG acts as the cold source to transfer the cold energy to the working fluid, so the condensing temperature of the working fluid determines the utilization rate of cold energy. The gasification curve of LNG can match better with the condensation curve of working fluid by using the non-azeotropic organic working fluid because of its temperature slip characteristic during phase transition. Liu and Guo [14] proposed a novel cryogenic cycle by using a binary mixture (CF_4 and C_3H_8) as the working fluid combined with the steam absorption process. The results showed that the model is significantly better than the ORC system using propane as the working medium, with an efficiency improvement of 66.3%. Mosaffa and Farshi [15] studied the performance of different non-azeotrope mixtures in an organic Rankine system combining solar energy and LNG cold energy. The results showed that R245ca/R236ea with a mass fraction of 0.6/0.4 had the best performance.

The phase transition is one of the important energy transfer modes for the working fluid in the thermodynamics cycles. Therefore, uncovering the phase transition mechanism of pure working fluids and their mixtures is of great significance for improving the thermal efficiency of the cycle and reducing the cost. At present, the researches on the interfacial phase transition of alkane working fluids are mainly through experiments [16-18]. And the molecular dynamics (MD) simulation method has been proved to be a powerful tool to reveal the micro/nano-mechanism of phase transition [19, 20]. For example, Liang et al. [21] used MD to study the evaporation behavior of Ar within a planar nanochannel. They controlled the steady-state evaporation flux by adjusting the temperature difference between the evaporating and condensing surfaces, and calculated the heat transfer coefficient at the gas-liquid interface. Pu et al. [22] studied the evaporation behavior of nanofilms on the surface of nanocolumns. The results showed that in order to maintain effective evaporation and avoid the inhibition of evaporation by separation pressure during evaporation, the thickness of the nanoscale liquid film should exceed the threshold at which capillary pressure begins to take effect. However, the microscopic phase transition mechanism of working fluids for LNG cold energy utilization ORC systems still need further investigation.

Consequently, in this paper, the interfacial evaporation process of ethane, propane and their different proportional mixtures on Cu substrate was simulated by MD. The interfacial tension, self-diffusion coefficient, and intermolecular interactions are discussed. This study aims to explore the microscopic phase transition mechanisms of the employed working fluid for their potential utilization in cold energy utilization ORC systems.

2. Methodology

2.1. Simulation models

In order to investigate the fluid-solid interfacial behavior of ethane, propane and their mixed working fluids during the phase transition, the initial model of mixtures (mass ratio 1:1) is shown as example in Fig.1. The model consists of two copper surfaces and a liquid film. The simulation box applied periodic boundary conditions in the X and Y directions and non-periodic boundary conditions in the Z direction. The dimensions of X, Y and Z are 5.422 nm, 5.422 nm and 60 nm respectively. The copper surface is composed of a face-centered cubic crystal structure (FCC) with a thickness of 2.168 nm. The liquid film here is composed of 900 ethane molecules and 614 propane molecules (the composition of the other working fluid systems is shown in Table 1). The bottom copper surface is divided into heat transfer layer, temperature control layer and fixed layer from top to bottom, and the top copper surface is set opposite to the bottom surface. Among them, the fixed layer can prevent the drift of the surface, the temperature control layer is used to control the temperature of the surface, and the heat transfer layer transfers the heat from the temperature control layer to the liquid film. Specifically, during the phase transition, the heat generated by the temperature control layer is transferred by the heat transfer layer to the liquid film region. Evaporation is triggered when the liquid film temperature rises. In the process of evaporation, the liquid alkane molecules enter the steam zone from the liquid film and condense on the surface when they reach the top copper region. Therefore, a long period of dynamic and stable evaporation stage can be formed without being hindered by vapor saturation pressure, which is convenient to study the evaporation process of liquid film. Due to the distance between the top surface and the liquid region is relatively long, the cold surface has no additional influence on the evaporation process studied.

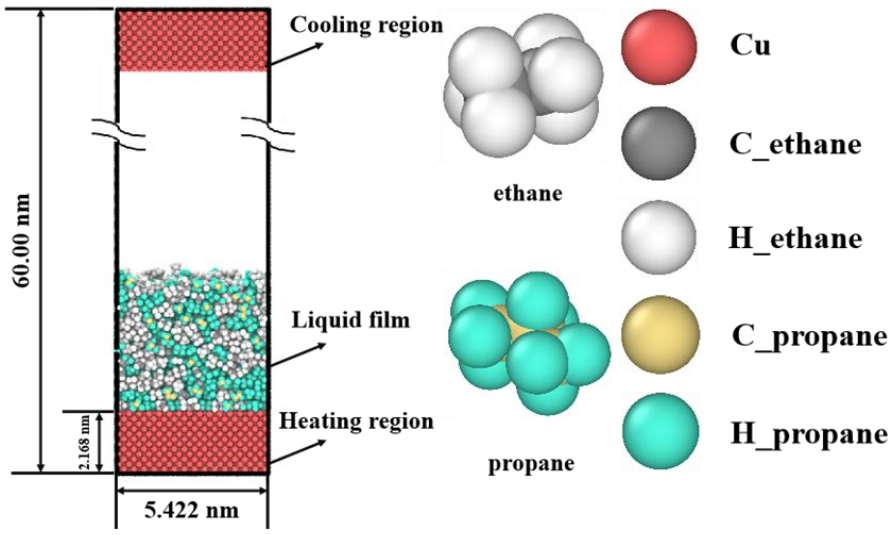

Figure 1. Initial model of evaporation system

In this study, the Lennard-Jones (12-6) potential is used to describe the interaction between copper atoms. The accuracy of this potential has been confirmed by previous work [23], and the specific parameters are: ε_{Cu}=4.72 kcal/mol, r_{Cu}=2.616Å. The force field parameters of alkanes are described by the OPLS-AA force field [24], which was developed by Jorgensen's team and subsequently modified for methane, ethane and other saturated alkanes [25], which can better simulate the thermodynamic properties of saturated alkanes. In addition, the cutoff distance of the

intermolecular interaction is 12 Å, and the parameters of the non-bonding interaction between different kinds of atoms are calculated using the Lorentz-Berthelot combination rule [26]. The long-distance Coulomb interaction is calculated using the particle-particle/particle mesh (PPPM) method [27].

Table 1. Liquid film composition of each system

Working fluid	Number of ethane	Number of propane
Pure ethane	1800	0
75% ethane	1350	307
50% ethane	900	614
25% ethane	450	921
Pure propane	0	1228

2.2. Simulation details

Here, the large-scale atomic/molecular massively parallel simulator (LAMMPS) [28] was used to study the molecular dynamics of alkane evaporation. OVITO software [29] was used to visualize the model and research process. The whole simulation is divided into two steps: equilibrium and evaporation. In the equilibrium process, the whole system adopts NVT ensemble to control the temperature at 140 K, to ensure that the alkane molecule in each system is in the liquid phase. The simulation time and time step of the equilibrium process are 1 ns and 1 fs, respectively. Based on the stable configuration obtained by the equilibrium process, the MD of the evaporation process of ethane, propane and their mixed working fluid was carried out. The Langevin thermostat was used to heat the bottom heating layer, and the temperature of the heating layer was maintained at 250 K. In addition, Langevin thermostat was also used to control the temperature of the top cooling layer at 140 K, with a time step of 1 fs and a simulation time of 10 ns to ensure the completion of the evaporation process.

In order to verify the accuracy of the simulation method in this study, simulations were conducted to confirm the densities of ethane and propane at temperatures between 130 and 180 K (with 10 K intervals) and a pressure of 1 MPa. The simulations were conducted using the NPT ensemble. The number of ethane and propane molecules was set to 2000 in each case, and the densities of the initial models for the NPT simulations were both set to 0.6 g/cm³. The time step was set to 1 fs, and the duration of the simulation was 1 ns. Simulated equilibrated densities of ethane and propane were compared with the data in REFPROP, and the maximum error was less than 2%, as is shown in Fig.2. It denotes that the force field parameters and MD code used here are reliable.

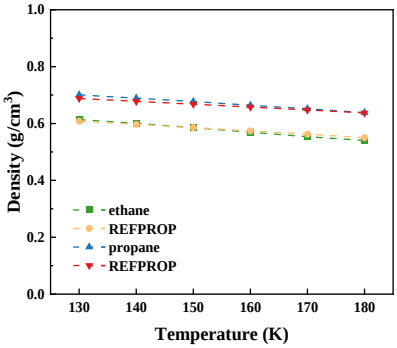

Figure 2. Comparison of simulated alkanes density with experimental data

3. Results and discussion

3.1. Evaporation process

Fig.3 shows the evaporation process of ethane, propane and their mixed working fluid. It can be seen from the figure that the evaporation process of each model has been completed at 10ns. In order to quantify the evaporation behavior of alkane molecules, the number of evaporating molecules was defined and calculated. As shown in Fig.4, in the evaporation process, the simulation system can be divided into bulk vapor, vapor-liquid interface, bulk liquid and liquid-solid interface. In this paper, the average density of the L-V interface (calculated as the arithmetic mean of the saturated liquid-phase density and the saturated gas-phase density) [19] is employed to ascertain the position of the L-V interface within the simulated system. The three-dimensional surface constituted by all points within the system with a density value equal to the aforementioned average density represents the L-V interface. The number of molecules evaporated is defined as the molecules passing through the vapor-liquid interface into the bulk vapor region. Fig.5 shows the relative molecular vaporization over time during the evaporation of studied systems. The relative molecular vaporization represents the fraction of molecules that have evaporated.

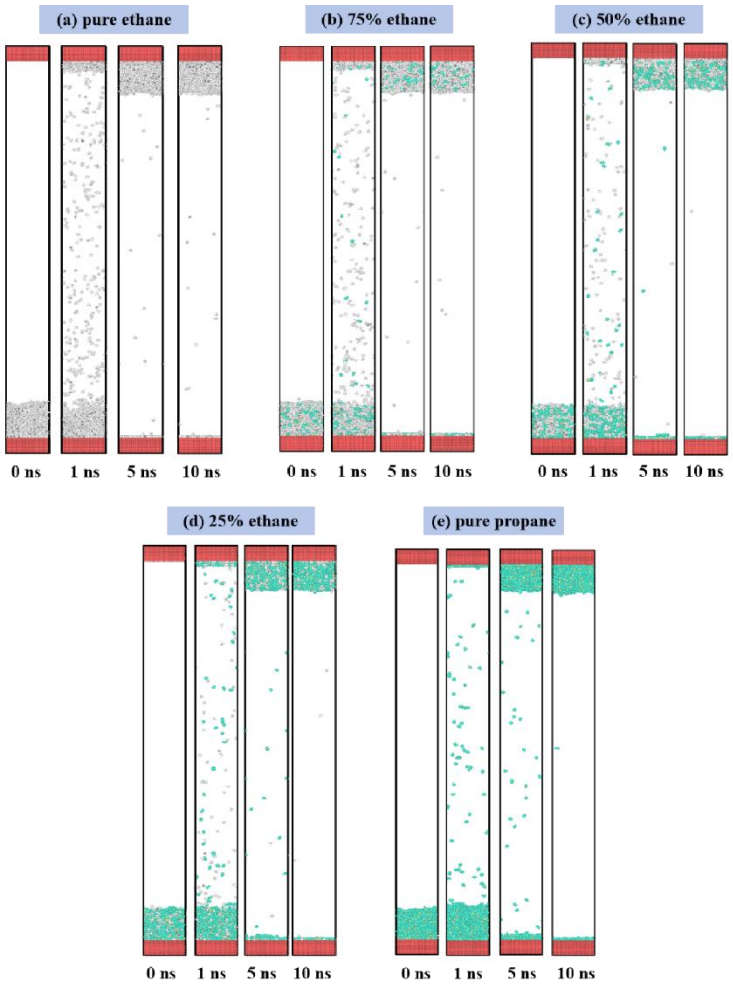

Figure 3. The snapshots of the studied system during the evaporation processes

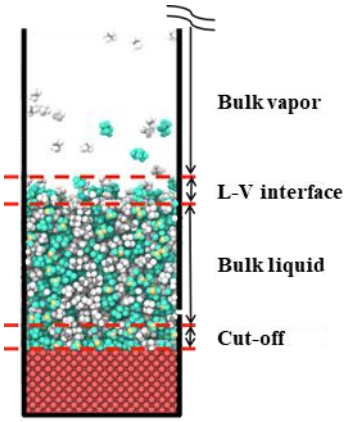

Figure 4. Schematic diagram of each area during the evaporation process

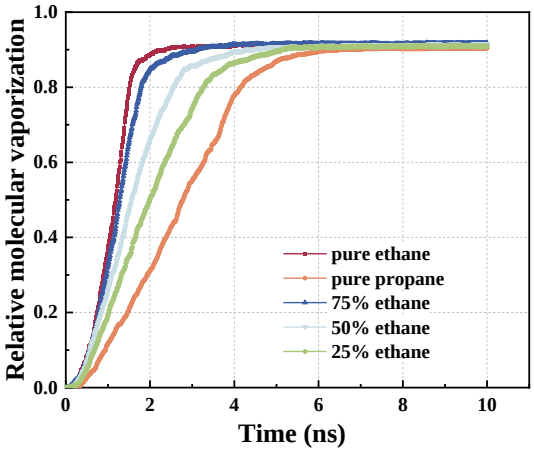

Figure 5. Relative molecular vaporization over time

It can be seen from the figure that in the first 0.5 ns of the simulation, the number of evaporated molecules increases slowly with the progress of the simulation, which is called the "initial stage". In the initial stage, the alkane molecules absorb heat from the Cu surface, and the liquid film temperature gradually increases. When the heat absorption reaches a certain value, the simulation system enters the next stage, the "stable evaporation stage", in which the alkane molecules are steadily evaporated, and the slope of the curve of the number of evaporated molecules remains almost unchanged. After the stability stage, the slopes of each evaporation molecular number curve decrease with time and gradually approach zero, which indicates that the evaporation process is inhibited. This is due to the strong interaction between the Cu surface and the liquid film near this surface. With the process of evaporation, the thickness of alkane liquid film decreases gradually. When the thickness of the liquid film is lower than a certain value, the liquid film is firmly attracted by the Cu surface, and its own evaporation is inhibited. The simulation snapshot also supports this. When the simulation ends, a layer of liquid molecules is firmly adsorbed on the surface, which is called the non-evaporative layer. In order to quantitatively calculate the rate of evaporation of the studied systems during the evaporation process, the evaporation rate of each simulation system is obtained according to the slope of the "stable stage", and the calculation formula is as follows [30]:

$$V = \frac{1}{A}\frac{M_L}{N_{AV}}\frac{\partial N_L}{\partial \tau} \quad (1)$$

In the formula, A is the cross-sectional area of X and Y direction, M_L and N_{AV} are the molar mass and Avogadro constant of the alkane molecule respectively, N_L is the number of liquid molecules, and τ is the simulation time. As is shown in Fig.6, the evaporation rates of each simulated system are as follows: pure ethane: 2437.66 kg/(m^2•s), 75% ethane: 1861.13 kg/(m^2•s), 50% ethane: 1175.62 kg/(m^2•s), 25% ethane: 871.69 kg/(m^2•s), pure propane: 667.74 kg/(m^2•s). The results indicate that the evaporation rate of pure ethane system is the highest, and that of pure propane system is the lowest. The higher the mass fraction of ethane, the higher the evaporation rate in the stable evaporation stage. It can be inferred that the existence of ethane improves the evaporation capacity of ethane/propane mixed working fluid system.

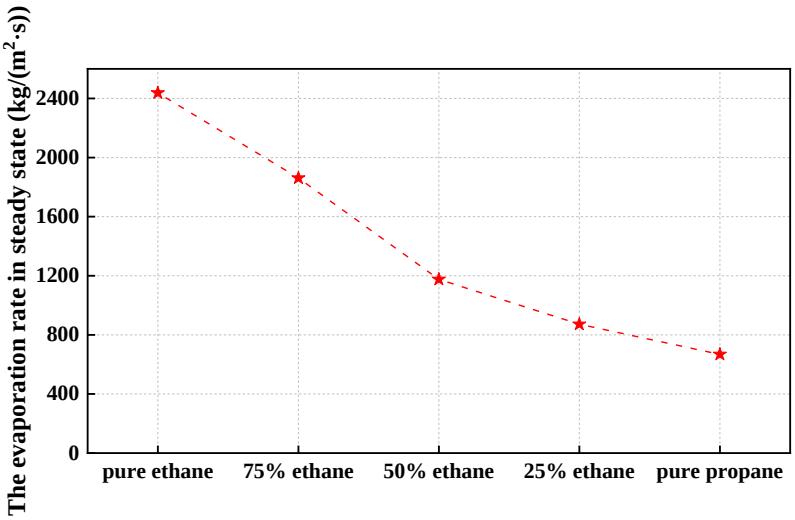

Figure 6. The evaporation rate of each system

In order to further understand the changes of each component in the ethane/propane mixed working fluid during evaporation, the changes of each component in the mixture over time were calculated, and the results were shown in Fig.7. It can be seen that in each system, the ethane in the component completes the evaporation process at about 3 ns, while the propane completes the evaporation process at about 6 ns. The proportion of propane in the final non-evaporable layer is higher than that of ethane (propane: 10%-13%, ethane: 6%-9%). This denotes that with the increase of ethane mass fraction in liquid film, the evaporation rate becomes faster, but the residual non-evaporable ethane molecules are also more. In other words, the addition of ethane obviously drives the evaporation of propane, and the higher the proportion of ethane, the faster the evaporation rate of propane.

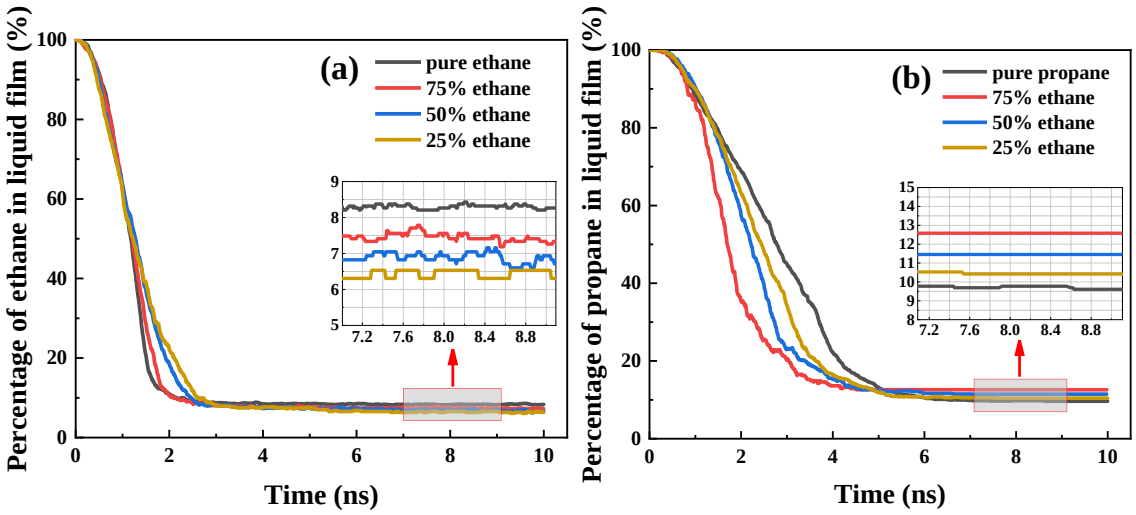

Figure 7. The change of each component in the working fluid during the evaporation process

3.2. Thermal resistance

Since the evaporation rate remains constant during the steady evaporation phase, further investigation into the stable evaporation period (1-1.5 ns) of each system was discussed in this section. In the evaporation process, thermal resistance has a great influence on interfacial heat transfer. For the studied system here, thermal resistance can be divided into solid thermal resistance (R_S), solid-liquid interface thermal resistance (R_{SL}), liquid thermal resistance (R_L) and gas-liquid interface thermal resistance (R_{LV}) [30]. Because the simulation parameters of the solid surface in different systems are the same and the temperature difference between the two sides of the thermal conductivity layer is small, the thermal resistance of the solid heat conduction in this paper can be ignored. Temperature difference and heat flux are used to define the thermal resistance of each part of the system,

$$R_{tot} = \frac{\left(T_S - T_V\right)}{q''} = R_{SL} + R_L + R_{LV} \tag{2}$$

$$R_{SL} = \frac{\left(T_S - T_{SL}\right)}{q''} \tag{3}$$

$$R_L = \frac{\left(T_{SL} - T_{LV}\right)}{q''} \tag{4}$$

$$R_{LV} = \frac{\left(T_{LV} - T_V\right)}{q''} \tag{5}$$

$$q'' = \frac{\partial \left| Q_{bottom} - Q_{top} \right|}{A \partial t} \tag{6}$$

where q''represents heat flux, T_{SL}, T_{LV} and T_V respectively represent the solid-liquid interface, gas-liquid interface and vapor phase temperature. The heat flux in the z-direction can be obtained from the slope of the cumulative energy difference of the Langevin temperature control layer in the bottom heat

source and the top heat sink with respect to time and the cross-sectional area of the wall, as shown in Eq. (6). And the temperature values represent time-averaged spatial statistical means for the respective regions. Where the time average is selected for the stable evaporation stage of the respective system. Due to the existence of mass flux of molecules in the vapor region in the z direction, the vapor phase temperature is only calculated in the X and Y directions, without considering the degrees of freedom in the Z direction [31]. Then, the thermal resistance of each system is calculated, and as shown in Fig.8. The results show that the total thermal resistance of ethane is smaller than that of propane, which results in a higher evaporation rate of ethane than propane. In addition, adding ethane to propane can significantly reduce the total thermal resistance of the system, the reduction effect becomes more obvious with the increase of the mass fraction of ethane. Moreover, the thermal resistance of the solid-liquid interface only accounts for a small part of the total thermal resistance. And the thermal resistance of the liquid phase does not simply increase with the increase of the mass fraction of propane, it is also related to the liquid film thickness. The density of propane is higher than that of ethane, results in the corresponding liquid film thickness of propane is lower than that of ethane. In each system, the thermal resistance of gas-liquid interface is higher than that of other interfaces, which indicates that the gas-liquid interface is an important factor affecting the interfacial evaporation process. The gas-liquid interface thermal resistance of pure propane is much higher than that of other systems, so pure propane system has the highest total thermal resistance.

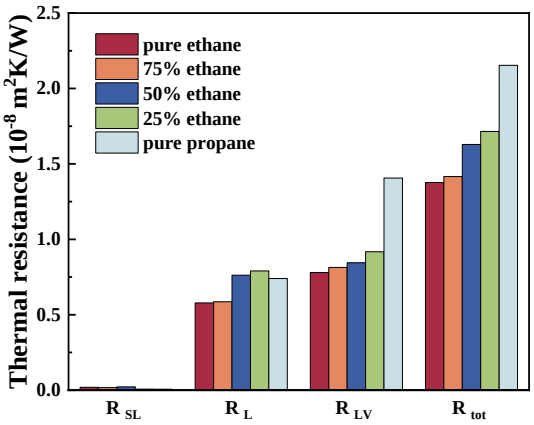

Figure 8. Thermal resistance of each simulated system

3.3. Discussion about other properties related to the phase transition

Since the evaporation process is dynamic, some important properties such as surface tension in the evaporation process cannot be obtained. Therefore, equilibrium molecular dynamics (EMD) simulation method is employed to investigate properties such as surface tension, molecular interaction energy, etc.

3.3.1 Surface tension

Surface tension γ is the energy required to increase the unit area of a surface [32], which means that a higher surface tension usually represents a stronger cohesive force. Surface tension γ can be obtained by integrating the difference between the normal pressure component (P_N) and the tangential pressure component (P_T) at the gas-liquid interface [20] as shown in Eq. (7). The initial model, as shown in Fig.9, consists of a liquid film located in the middle and two vacuum layers. The dimensions

of the simulation box in the X, Y, and Z directions are 5.422 nm, 5.422 nm, and 20.00 nm, respectively. The number of molecules in the liquid film is the same as that in the liquid film of evaporation process.

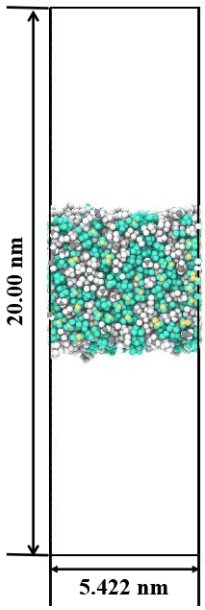

Figure 9. Initial model of surface tension

$$\gamma = \frac{1}{2} \int_0^{L_z} \left[P_N(z) - P_T(z) \right] dz \tag{7}$$

The surface tension simulation process is also divided into two steps: equilibrium and calculation, both using NVT ensemble, with time step of 1 fs and the cutoff distance of the intermolecular interaction is 12 Å. During the equilibrium process, the Nose-Hoover thermostat was used to gradually heat the system temperature from 100 K to 140 K, and the simulation time was 0.5 ns. Subsequently, an equilibrium simulation of 1.5 ns was conducted in the NVT ensemble, with the final 1 ns employed for data acquisition. The surface tension was statistically calculated, as shown in Fig.10.

The surface tension in ascending order is as follows: pure ethane, 75% ethane, 50% ethane, 25% ethane, and pure propane. As the surface tension increases, the energy required for liquid molecules to escape from the gas-liquid interface into the gas phase also increases. This indicates that ethane has the smallest evaporative energy barrier, while propane has the largest evaporative energy barrier. The surface tension of the mixed working fluids increases with the increase in the mass fraction of ethane.

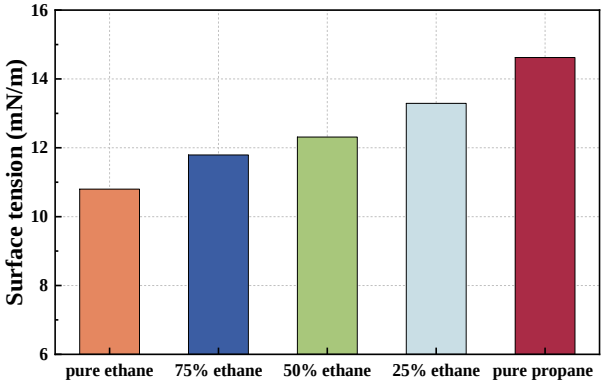

Figure 10. Surface tension of each working fluid

3.3.2 Diffusion properties

Evaporation is a heat and mass transfer process, it is also influenced by the properties of the liquid molecules, such as the self-diffusion coefficient and molecular interaction energy. To calculate the properties of the liquid molecules on the Cu surface, an initial simulation model was constructed as shown in Fig.11. The dimensions of the simulation box in the X, Y, and Z directions are 5.422 nm, 5.422 nm, and 10.00 nm, respectively. The composition of liquid film and Cu layer is the same as that of evaporation process model. The simulation process adopts NVT ensemble, the system temperature is set to 140 K, the time step is 1 fs. The equilibrium process of 0.5 ns is performed first, and then the calculation process of 4 ns is performed. The self-diffusion coefficient can be calculated by the mean square displacement (MSD) [33],

$$MSD = \left\langle \left| r(t) - r(0) \right|^2 \right\rangle \tag{8}$$

$$D = \lim_{t \to \infty} \frac{1}{6t} MSD \tag{9}$$

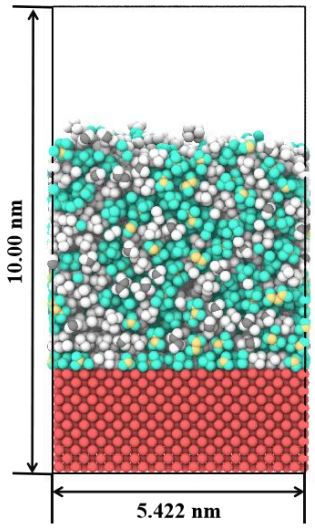

Figure 11. Initial model of diffusion properties

The calculated self-diffusion coefficient of each system is shown in Fig.12(a). In this paper, the calculation of the diffusion coefficient employed MSD of the center of mass of the molecule. The self-

diffusion coefficient of ethane liquid molecules on Cu surface is the highest, while that of propane liquid is the lowest. And it increases with the increase of ethane mass fraction. The high diffusion capacity of liquid molecules on the solid surface can improve its own evaporation performance. In order to further explore the influence of each component in the mixed working fluid on the self-diffusion coefficient, the respective self-diffusion coefficients of ethane and propane in the mixture were also calculated, as shown in Fig.12(b). The self-diffusion coefficient of ethane is higher than that of propane, which also indicates that ethane molecules are less restricted in the liquid interior. In the mixed system, the self-diffusion coefficient of ethane molecules also decreases with the decrease of ethane mass fraction. For propane, the addition of ethane enhanced the diffusion ability of propane in the liquid film, and the enhancement effect was more significant with the increase of ethane mass fraction.

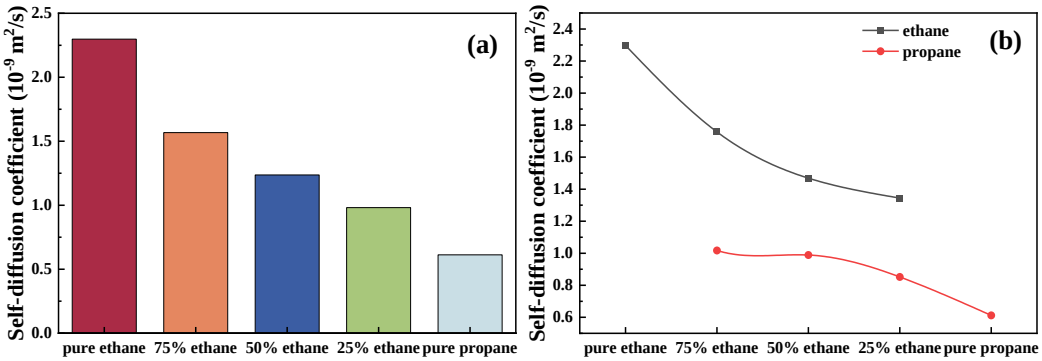

Figure 12. (a) self-diffusion coefficient of each system (b) self-diffusion coefficient of each component in the mixed working fluid

3.3.3 Interaction energy

The interaction between molecules will also determine the evaporation properties of the fluid. According to the simulation model in the previous section, the interaction energy between molecules of the liquid is calculated as shown in Fig.13. It can be seen from the figure that the interaction energy of liquid film is all negative, indicating that the interaction force between liquid molecules is mainly attraction. The absolute value of the interaction energy represents the strength of the attraction, and the intermolecular attraction strength of ethane is the smallest, so it has the smallest resistance to break through the liquid zone into the gas phase zone, and has the smallest evaporation energy barrier. The addition of ethane in the mixed working fluid reduces the intermolecular force, so the evaporation rate of the mixture is higher than that of pure propane system.

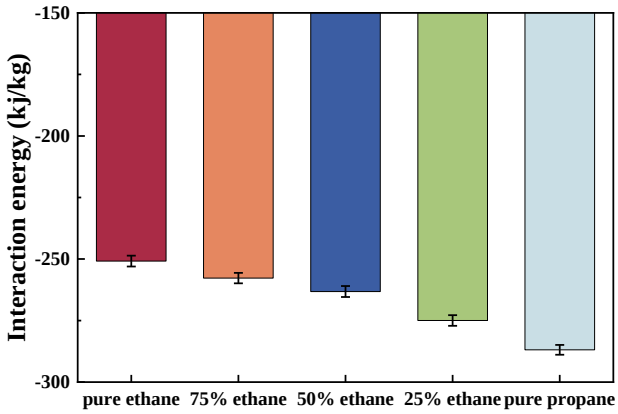

Figure 13. The Interaction energy of each working fluid

4. Conclusion

In this study, the interfacial evaporation process of ethane, propane and their mixed working fluid was investigated by MD. The main conclusions were as follows, in all systems, pure ethane has the highest evaporation rate, and the addition of ethane to the mixing medium can increase the evaporation rate of propane. The thermal resistance of gas-liquid interface accounts for a large proportion in the total thermal resistance, which is the main reason for the difference of thermal resistance. The surface tension and interaction energy of ethane system are small, which indicates that its evaporation energy barrier is also small, and ethane has the largest diffusion coefficient, which makes it have the largest evaporation rate.

Acknowledgment

This work is supported by the Natural Science Foundation of Chongqing (CSTB2023TIAD-KPX0087).

References

[1] Burel, F., *et al.*, Improving sustainability of maritime transport through utilization of Liquefied Natural Gas (LNG) for propulsion, *Energy*, *57* (2013), pp. 412-420, DOI No. https://doi.org/10.1016/j.energy.2013.05.002

[2] Kumar, S., *et al.*, LNG: An eco-friendly cryogenic fuel for sustainable development, *Applied Energy*, *88* (2011), 12, pp. 4264-4273, DOI No. https://doi.org/10.1016/j.apenergy.2011.06.035

[3] Wang, S., *et al.*, Selection principle of working fluid for organic Rankine cycle based on environmental benefits and economic performance, *Applied Thermal Engineering*, *178* (2020), p. 115598, DOI No. https://doi.org/10.1016/j.applthermaleng.2020.115598

[4] Cao, W., *et al.*, Theoretical approach of freeze seawater desalination on flake ice maker utilizing LNG cold energy, *Desalination*, *355* (2015), pp. 22-32, DOI No. https://doi.org/10.1016/j.desal.2014.09.034

[5] Ghaebi, H., *et al.*, Energy, exergy and thermoeconomic analysis of a novel combined cooling and power system using low-temperature heat source and LNG cold energy recovery, *Energy*

Conversion and Management, *150* (2017), pp. 678-692, DOI No. https://doi.org/10.1016/j.enconman.2017.08.052

[6] Mehrpooya, M., *et al.*, Optimum design and exergy analysis of a novel cryogenic air separation process with LNG (liquefied natural gas) cold energy utilization, *Energy*, *90* (2015), pp. 2047-2069, DOI No. https://doi.org/10.1016/j.energy.2015.07.101

[7] Al-musleh, E. I., *et al.*, Efficient electrochemical refrigeration power plant using natural gas with ∼100% CO2 capture, *Journal of Power Sources*, *274* (2015), pp. 130-141, DOI No. https://doi.org/10.1016/j.jpowsour.2014.09.184

[8] Yao, S. G., *et al.*, Design study on the integrated utilization system of medium-temperature waste heat and LNG vaporization cold energy for 200,000 DWT LNG-powered vessels, *Thermal Science*, *27* (2023), 2A, pp. 1289-1299, DOI No. 10.2298/TSCI220326146Y

[9] Jovijari, F., *et al.*, Advanced exergy analysis of the natural gas liquid recovery process, *Thermal Science*, *26* (2022), 3, pp. 2287-2300, DOI No. 10.2298/TSCI210522311J

[10] He, T., *et al.*, LNG cold energy utilization: Prospects and challenges, *Energy*, *170* (2019), pp. 557-568, DOI No. https://doi.org/10.1016/j.energy.2018.12.170

[11] Sun, Z., *et al.*, Thermodynamic optimization and comparative study of different ORC configurations utilizing the exergies of LNG and low grade heat of different temperatures, *Energy*, *147* (2018), pp. 688-700, DOI No. https://doi.org/10.1016/j.energy.2018.01.085

[12] Arcuri, N., *et al.*, LNG as cold heat source in OTEC systems, *Ocean Engineering*, *104* (2015), pp. 349-358, DOI No. https://doi.org/10.1016/j.oceaneng.2015.05.030

[13] Lee, S., Multi-parameter optimization of cold energy recovery in cascade Rankine cycle for LNG regasification using genetic algorithm, *Energy*, *118* (2017), pp. 776-782, DOI No. https://doi.org/10.1016/j.energy.2016.10.118

[14] Liu, Y.,K. Guo, A novel cryogenic power cycle for LNG cold energy recovery, *Energy*, *36* (2011), 5, pp. 2828-2833, DOI No. https://doi.org/10.1016/j.energy.2011.02.024

[15] Mosaffa, A. H., Farshi, L. G., Thermodynamic feasibility evaluation of an innovative salinity gradient solar ponds-based ORC using a zeotropic mixture as working fluid and LNG cold energy, *Applied Thermal Engineering*, *186* (2021), 116488, DOI No. https://doi.org/10.1016/j.applthermaleng.2020.116488

[16] Hillenbrand, T., Brüggemann, D., Evaporation of free falling droplets of binary alkane-ethanol blends, *Fuel*, *274* (2020), 117869, DOI No. https://doi.org/10.1016/j.fuel.2020.117869

[17] Zuo, Z., *et al.*, Experimental investigation on energy and mass transport at steady-state evaporating interface in liquid methane storage tanks, *Applied Thermal Engineering*, *226* (2023), 120258, DOI No. https://doi.org/10.1016/j.applthermaleng.2023.120258

[18] Zhan, J., *et al.*, Experimental study of ethane pulsating heat pipe with varying evaporator lengths based on pulse tube refrigerator, *International Journal of Refrigeration*, *145* (2023), pp. 40-49, DOI No. https://doi.org/10.1016/j.ijrefrig.2022.09.010

[19] Deng, X., *et al.*, Evaporation of R1234yf, R1234ze(E) and R1234ze(Z) on Cu surface: A molecular dynamics study, *Journal of Molecular Liquids*, *344* (2021), 117844, DOI No. https://doi.org/10.1016/j.molliq.2021.117844

[20] Li, Y., *et al.*, Interfacial anomaly in low global warming potential refrigerant blends as predicted by molecular dynamics simulations, *Physical Chemistry Chemical Physics*, *21* (2019), 39, pp. 22092-22102, DOI No. 10.1039/C9CP03231B

[21] Liang, Z., *et al.*, Molecular simulation of steady-state evaporation and condensation: Validity of the Schrage relationships, *International Journal of Heat and Mass Transfer*, *114* (2017), pp. 105-114, DOI No. https://doi.org/10.1016/j.ijheatmasstransfer.2017.06.025

[22] Pu, J. H., *et al.*, Stable and Efficient Nanofilm Pure Evaporation on Nanopillar Surfaces, *Langmuir*, *37* (2021), 12, pp. 3731-3739, DOI No. 10.1021/acs.langmuir.1c00236

[23] Heinz, H., *et al.*, Accurate Simulation of Surfaces and Interfaces of Face-Centered Cubic Metals Using 12−6 and 9−6 Lennard-Jones Potentials, *The Journal of Physical Chemistry C*, *112* (2008), 44, pp. 17281-17290, DOI No. 10.1021/jp801931d

[24] Jorgensen, W. L., *et al.*, Optimized intermolecular potential functions for liquid hydrocarbons, *Journal of the American Chemical Society*, *106* (1984), pp. 6638-6646

[25] Kaminski, G., *et al.*, Free Energies of Hydration and Pure Liquid Properties of Hydrocarbons from the OPLS All-Atom Model, *The Journal of Physical Chemistry*, *98* (1994), 49, pp. 13077-13082, DOI No. 10.1021/j100100a043

[26] Delhommelle, J.,P. MilliÉ, Inadequacy of the Lorentz-Berthelot combining rules for accurate predictions of equilibrium properties by molecular simulation, *Molecular Physics*, *99* (2001), 8, pp. 619-625, DOI No. 10.1080/00268970010020041

[27] Hockney, R.W., *et al.*, Quiet high-resolution computer models of a plasma, *Journal of Computational Physics*, *14* (1974), 2, pp. 148-158, DOI No. https://doi.org/10.1016/0021-9991(74)90010-2

[28] Plimpton, S., Fast Parallel Algorithms for Short-Range Molecular Dynamics, *Journal of Computational Physics*, *117* (1995), 1, pp. 1-19, DOI No. https://doi.org/10.1006/jcph.1995.1039

[29] Stukowski, A., Visualization and analysis of atomistic simulation data with OVITO–the Open Visualization Tool, *Modelling and Simulation in Materials Science and Engineering*, *18* (2010), 1, p. 015012, DOI No. 10.1088/0965-0393/18/1/015012

[30] Montazeri, K., *et al.*, Solid-like Behaviors Govern Evaporative Transport in Adsorbed Water Nanofilms, *ACS Applied Materials & Interfaces*, *12* (2020), 47, pp. 53416-53424, DOI No. 10.1021/acsami.0c13647

[31] Gatapova, E. Y., *et al.*, The temperature and pressure jumps at the vapor–liquid interface: Application to a two-phase cooling system, *International Journal of Heat and Mass Transfer*, *83* (2015), pp. 235-243

[32] Yong, X., *et al.*, Nanoparticle-mediated evaporation at liquid–vapor interfaces, *Extreme Mechanics Letters*, *7* (2016), pp. 90-103, DOI No. https://doi.org/10.1016/j.eml.2016.04.001

[33] Topping, J., Investigations on the Theory of the Brownian Movement, *Physics Bulletin*, *7* (1956), 10, p. 281, DOI No. 10.1088/0031-9112/7/10/012

Received: 19.08.2024.
Revised: 21.10.2024.
Accepted: 24.10.2024.